

# A statistically selected *Chandra* sample of 20 galaxy clusters – I. Temperature and cooling time profiles

Alastair J. R. Sanderson,<sup>1,2\*</sup> Trevor J. Ponman<sup>1</sup> and Ewan O’Sullivan<sup>3</sup>

<sup>1</sup>*School of Physics and Astronomy, University of Birmingham, Edgbaston, Birmingham B15 2TT*

<sup>2</sup>*Department of Astronomy, University of Illinois, 1002 West Green Street, Urbana, IL 61801, USA*

<sup>3</sup>*Harvard-Smithsonian Center for Astrophysics, 60 Garden Street, Cambridge, MA 02138, USA*

Accepted 2006 August 18. Received 2006 August 18; in original form 2006 May 24

## ABSTRACT

We present an analysis of 20 galaxy clusters observed with the *Chandra* X-ray satellite, focusing on the temperature structure of the intracluster medium and the cooling time of the gas. Our sample is drawn from a flux-limited catalogue but excludes the Fornax, Coma and Centaurus clusters, owing to their large angular size compared to the *Chandra* field of view. We describe a quantitative measure of the impact of central cooling, and find that the sample comprises nine clusters possessing cool cores (CCs) and 11 without. The properties of these two types differ markedly, but there is a high degree of uniformity amongst the CC clusters, which obey a nearly universal radial scaling in temperature of the form  $T \propto r^{-0.4}$ , within the core. This uniformity persists in the gas cooling time, which varies more strongly with radius in CC clusters ( $t_{\text{cool}} \propto r^{-1.3}$ ), reaching  $t_{\text{cool}} < 1$  Gyr in all cases, although surprisingly low central cooling times ( $< 5$  Gyr) are found in many of the non-CC systems. The scatter between the cooling time profiles of all the clusters is found to be remarkably small, implying a universal form for the cooling time of gas at a given physical radius in virialized systems, in agreement with recent previous work. Our results favour cluster merging as the primary factor in preventing the formation of CCs.

**Key words:** galaxies: clusters: general – intergalactic medium – X-rays: galaxies: clusters.

## 1 INTRODUCTION

Clusters of galaxies are uniquely suitable environments for studying galaxy formation and evolution, as well as excellent cosmological tools for measuring the fundamental parameters of the Universe. A study of the scaling properties of clusters, which span roughly two decades in mass, is one of the best means of tackling both these objectives, and many analyses have been conducted on this basis, establishing broad trends and quantifying departures from simple self-similarity (e.g. Edge & Stewart 1991b; Markevitch et al. 1998; Helsdon & Ponman 2000; Fukazawa, Makishima & Ohashi 2004).

Increasingly, however, attention is shifting towards a more complete understanding of cluster physics, focusing in particular on the scatter in these scaling relations. With current generation telescopes, we are reaching the point where the precision of scaling relations is limited by systematic effects rather than measurement errors. Further progress requires a better knowledge of cluster physics to understand the sources of intrinsic scatter in these relations. Not only does this hold great potential for understanding galaxy evolution, but it also promises to hone cluster observables as proxies for mass,

which will be vital in extracting precise cosmological constraints from forthcoming large cluster surveys.

Since the cooling time of gas in the centres of most clusters is short compared to their age, radiative cooling would be expected to play an important role in cluster physics. However, many clusters do not show strong signs of cooling, possibly as a result of disruption caused by merging and associated shock heating of the gas, or else non-gravitational energy input [e.g. from active galactic nuclei (AGN)], or even heat redistribution via conduction or mixing. Moreover, even where cooling dominates, its progress is apparently impeded (see the recent review by Peterson & Fabian 2006, and references therein), by processes which may well relate to these same phenomena. Whatever be the explanation, it is clear that clusters can be separated into two distinct categories, according to the presence or absence of a ‘cool core (CC)’ (Peres et al. 1998; Bauer et al. 2005), where radiative heat losses have significantly lowered the central temperature of the gas. It is the combination of CC and non-CC systems in the cluster population which accounts for much of the intrinsic scatter in scaling relations.

While CC clusters have tended to be relatively well-studied, non-CC clusters have received less attention in scaling relation analyses. Consequently, there is great potential for exploring cluster physics by comparing the properties of the two types of clusters. This aim of this work is to investigate precisely this comparison, by focusing

\*E-mail: ajrs@star.sr.bham.ac.uk

**Table 1.** Some basic properties of the sample, listed in order of increasing temperature. Coordinates are the centroids used in the X-ray analysis.

Name	ObsID <sup>a</sup>	Detector <sup>b</sup>	RA (J2000)	Dec. (J2000)	Redshift	H I column <sup>c</sup> ( $\times 10^{20} \text{ cm}^{-2}$ )	Mean $kT^d$ (keV)	$r_{500}$ (kpc)	Notes <sup>e</sup>
NGC 5044	798	S	198.850	-16.385	0.008	4.9	1.19 <sup>+0.03</sup> <sub>-0.02</sub>	436	-
Abell 262	2215	S (VF)	28.194	36.152	0.016	5.4	2.34 <sup>+0.06</sup> <sub>-0.06</sub>	668	-
Abell 4038	4188	I (VF)	356.928	-28.143	0.030	1.6	3.02 <sup>+0.17</sup> <sub>-0.17</sub>	784	F, T
Abell 1060	2220	I (VF)	159.181	-27.526	0.012	4.8	3.19 <sup>+0.07</sup> <sub>-0.07</sub>	812	F, T
Abell 1367	514	S	176.191	19.699	0.022	2.3	3.28 <sup>+0.11</sup> <sub>-0.10</sub>	826	T
2A0335+096	919	S	54.669	9.970	0.035	17.9	3.47 <sup>+0.14</sup> <sub>-0.12</sub>	856	-
Abell 2147	3211	I (VF)	240.567	15.963	0.035	3.4	4.17 <sup>+0.14</sup> <sub>-0.14</sub>	961	F, T
Abell 2199	497	S	247.160	39.551	0.030	0.9	4.36 <sup>+0.13</sup> <sub>-0.11</sub>	989	-
Abell 496	931	S	68.408	-13.262	0.033	4.6	5.91 <sup>+0.58</sup> <sub>-0.56</sub>	1200	-
Abell 2256	1386	I	256.041	78.648	0.058	4.1	6.08 <sup>+0.30</sup> <sub>-0.31</sub>	1220	T
Abell 1795	493	S (VF)	207.219	26.590	0.062	1.2	6.30 <sup>+0.17</sup> <sub>-0.17</sub>	1250	-
Abell 3558	1646	S (VF)	201.987	-31.496	0.048	3.9	6.64 <sup>+0.34</sup> <sub>-0.51</sub>	1290	T
Abell 85	904	I	10.460	-9.303	0.059	3.4	6.65 <sup>+0.14</sup> <sub>-0.14</sub>	1290	-
Abell 3571	4203	S (VF)	206.869	-32.864	0.039	3.7	6.71 <sup>+0.15</sup> <sub>-0.42</sub>	1300	F, T
Abell 3667	889	I	303.129	-56.841	0.056	4.7	7.39 <sup>+0.27</sup> <sub>-0.27</sub>	1380	T
Abell 478	1669	S	63.356	10.466	0.088	15.1	7.97 <sup>+0.18</sup> <sub>-0.18</sub>	1450	-
Abell 401	518	I	44.739	13.578	0.074	10.5	8.35 <sup>+0.43</sup> <sub>-0.51</sub>	1490	T
Abell 2029	4977	S	227.734	5.745	0.077	3.0	9.11 <sup>+0.50</sup> <sub>-0.20</sub>	1570	-
Abell 2142	1196	S	239.585	27.232	0.091	4.2	9.45 <sup>+0.65</sup> <sub>-0.65</sub>	1610	-
Abell 3266	899	I (VF)	67.815	-61.456	0.055	1.6	9.86 <sup>+0.53</sup> <sub>-0.54</sub>	1650	F, T

<sup>a</sup>*Chandra* observation identifier. <sup>b</sup>Denotes either ACIS-I or ACIS-S (observations telemetred in VF mode are marked with VF). <sup>c</sup>Galactic H I column, interpolated to the cluster centroid using the data of Dickey & Lockman (1990). <sup>d</sup>The mean temperature measured between 0.1 and  $0.2r_{500}$  (see Section 4.1). <sup>e</sup>An ‘F’ indicates that the Galactic absorption was frozen at the H I value for the analysis, whereas ‘T’ marks those clusters for which the projected  $T(r)$  was used for the three-dimensional  $T(r)$ . All errors are 68 per cent confidence.

on a systematically selected sample of clusters, using data from the *Chandra* satellite, to allow a high-resolution study of the core properties of the intracluster medium (ICM).

Previous detailed studies of the temperature structure of the hot gas in clusters have generally concentrated on the most-relaxed (i.e. morphologically regular) clusters (e.g. Sanderson et al. 2003; Piffaretti et al. 2005; Vikhlinin et al. 2005), which frequently possess CCs. In this work, we have compiled a statistically selected sample of 20 clusters, to provide a more rigorous selection process. This naturally includes a larger number of non-CC and perhaps less-relaxed clusters, which are more representative of the cluster population as a whole. We have subjected these 20 systems to a non-parametric analysis, so as to avoid any model-dependent biases in the comparison of CC and non-CC systems. Furthermore, in restricting the analysis to X-ray data taken with the *Chandra* satellite, we are able to exploit the unrivalled spatial resolution of this telescope, to permit a detailed examination of the inner regions of the ICM, where the impact of radiative cooling is most pronounced.

Throughout this paper, we adopt the following cosmological parameters;  $H_0 = 70 \text{ km s}^{-1} \text{ Mpc}^{-1}$ ,  $\Omega_m = 0.3$  and  $\Omega_\Lambda = 0.7$ . Throughout our spectral analysis, we have used XSPEC v11.3.1, incorporating the solar abundance table of Grevesse & Sauval (1998), which is different from the default abundance table. Typically, this results in larger Fe abundances, by a factor of  $\sim 1.4$ . All errors are  $1\sigma$ , unless otherwise stated.

## 2 SAMPLE SELECTION AND PROPERTIES

The sample comprises the 20 highest flux clusters drawn from the 63 cluster, flux-limited sample of Ikebe et al. (2002), excluding those objects with extremely large angular sizes (the Coma, Fornax and Centaurus clusters), which are difficult to observe with

*Chandra*, owing to its limited field of view. Some basic properties of this sample are listed in Table 1. The Ikebe et al. flux-limited sample was constructed from the HIFLUGS sample of Reiprich & Böhringer (2002), additionally selecting clusters lying above an absolute Galactic latitude of  $20^\circ$  and located outside the Magellanic Clouds and the Virgo Cluster regions.

Fig. 1 shows the cluster redshift as a function of mean X-ray temperature, excluding any CC (see Section 4.1). The temperature errors are generally too small to be seen, and have been omitted for clarity. The point style differentiates between those clusters possessing a significant CC and those without. The CC classification scheme is described in Section 4.2.

## 3 DATA REDUCTION

The data analysis and reduction were performed with version 3.2.2 of the standard software – *Chandra* Interactive Analysis of Observations (CIAO<sup>1</sup>) incorporating CALDB version 3.1. For all the observations, a new level 2 events file was generated from the level 1 events file downloaded from the *Chandra* archive. This ensures that the latest calibration information is applied uniformly to the data, irrespective of when the observations were made.

The following procedure was followed for each observation data set. According to which CCD chips were used in the observation, a different light curve was extracted for CCD chips 5 and 7 separately and the remaining, front-illuminated chips combined. The recommended criteria for energy extraction and time binning were used.<sup>2</sup> Flares were identified and excluded with the sigma clipping

<sup>1</sup> <http://cxc.harvard.edu/ciao/>.

<sup>2</sup> <http://cxc.harvard.edu/contrib/maxim/bg>.

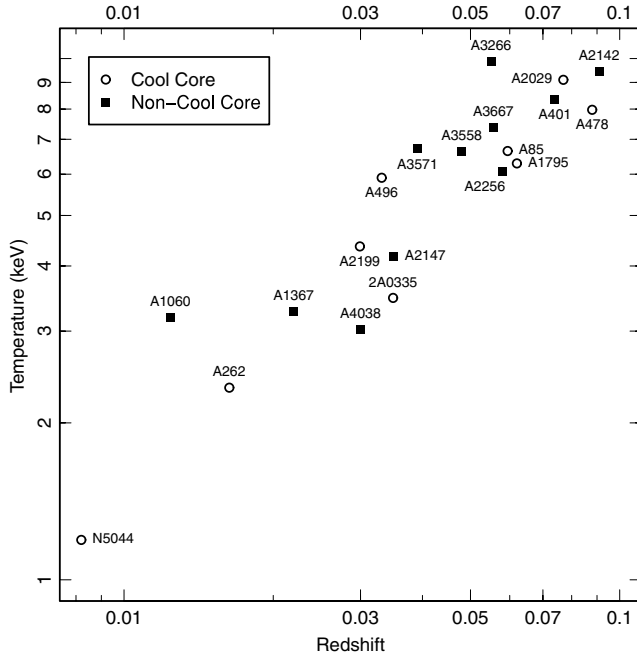


**Figure 1.** Cluster mean temperature within  $0.1-0.2r_{500}$  as a function of redshift, labelled according to the presence of a CC. Temperature errors have been omitted for clarity. Redshifts are taken from the NASA/IPAC Extragalactic Database (NED).

algorithm implemented in the CIAO task ‘LC\_CLEAN’, using the median light curve value to provide a robust initial estimate of the quiescent mean level.

Cosmic ray events were identified and excluded using the CIAO task ‘ACIS\_RUN\_HOTPIX’, and those found in this manner were extracted separately and examined to check that photons from the cluster itself were not misidentified. A new level 1 events file was produced by reprocessing the resulting events file, to apply the latest gain file. Corrections were applied for the effects of charge transfer inefficiency (CTI) and time-dependent gain variation, where necessary. Bad columns and hot pixels were then excluded, and only events with *Advanced Satellite for Cosmology and Astrophysics* (ASCA) grades 0, 2, 3, 4, and 6 were retained. Subsequently, a new level 2 events file was generated by reprocessing this modified level 1 events data set. For those observations telemetered in very faint (VF) mode (indicated in column 3 of Table 1), the extra background event flagging and removal that this enables was performed in both the main and corresponding blank-sky data sets.

Owing to the close proximity of the clusters in this sample, emission from the target fills the entire *Chandra* field of view in most cases. It was therefore necessary to employ separate background events files for each observation, using the Markevitch blank-sky data sets.<sup>3</sup> To allow for small variations in the particle background level between the blank-sky fields and the target observation, we rescaled the effective exposure of the background data sets according to the ratio of count rates in the particle-dominated 7–12 keV energy band. This ratio was calculated for those CCD chips not considered part of the main detector (i.e. excluding chips 0–3 for ACIS-I and chip 7 for ACIS-S observations). Generally, there is good agreement between the ratios found for different chips in a

given observation. To avoid the bias caused by contaminating point sources in the determination of the background rescale factors, we identified and excluded such features using the iterative method described in Sanderson, Finoguenov & Mohr (2005).

To gauge the sensitivity of our results to variations in the normalization of the blank-sky data sets, we investigated its impact on our analysis of Abell 4038 (mean temperature  $\sim 3$  keV) – the cluster most susceptible to this effect (i.e. where the background is most dominant). We refitted spectra from our annular profile (see Section 4.3), separately adjusting the background normalization by 10 per cent higher and lower. In the outermost annulus, this biased the recovered temperature by roughly  $1\sigma$ , in the direction of increasing temperature with higher background. However, the bias rapidly diminishes for the inner annuli, dropping below  $0.3\sigma$  for the third innermost spectrum. It is clear, therefore, that our results are not sensitive to uncertainties associated with the use of blank-sky background data sets.

## 4 DATA ANALYSIS

### 4.1 Cluster mean temperature and fiducial radius

The primary focus of this study is on cluster core properties, and we have therefore chosen to devote our analysis to the main CCD chips for each of the two detectors, that is, chips 0–3 for ACIS-I and chip 7 for ACIS-S. For the spectral fitting, weighted response matrix files (RMFs) were generated using the CIAO task ‘MKACISRMF’. However, for some observations this was not possible (as indicated in Section 5), owing to a lack of calibration data suitable for mkacisrmf, and so the older task ‘MKRMF’ was used instead. In each case, the correct gain file was used, appropriate as described in the CIAO documentation.

In a scaling study such as this, it is important to normalize observable quantities appropriately, to provide a fair comparison between clusters of different sizes. The key parameters of interest are mean gas temperature and characteristic radius, and we outline below a simple scheme in which both these quantities are determined self-consistently. Our fiducial radius corresponds to an overdensity of 500 with respect to the critical density of the Universe. This radius,  $r_{500}$ , is commonly used for scaling studies and corresponds to roughly two-thirds of  $r_{200}$  (Sanderson & Ponman 2003).

We defer a full mass profile analysis and direct determination of overdensity radii to a later paper, and adopt in this work a simple, empirically calibrated proxy for the total mass within  $r_{500}$ , based on the mean temperature, derived from the  $M-T_X$  relation of Finoguenov, Reiprich & Böhringer (2001). This has the advantage of permitting a direct comparison with other observations where poorer data quality prevents a full mass analysis being performed. For a cluster of redshift,  $z$ , the radius is given by (Willis et al. 2005):

$$r_{500} = \frac{391 \times \bar{T}^{0.63}}{E(z)} \text{ kpc}, \quad (1)$$

where

$$E(z) = (1+z) \sqrt{1 + (z \Omega_m) + \frac{\Omega_\Lambda}{(1+z)^2} - \Omega_\Lambda}. \quad (2)$$

In calibrating the temperature–radius relation using observed clusters, we avoid the bias inherent in equivalent relations derived from numerical simulations, which tend to overestimate the virial radii of the coolest haloes (Sanderson et al. 2003). In using the above

<sup>3</sup> <http://xcx.harvard.edu/contrib/maxim/acisbg>.

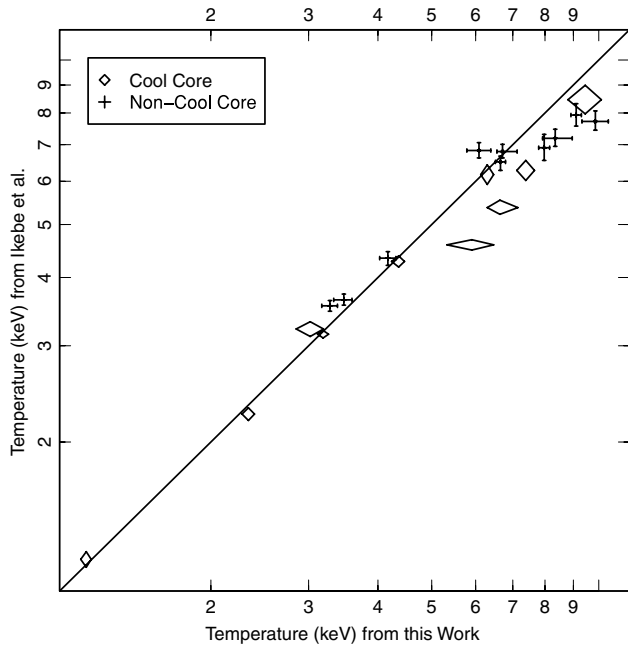


**Figure 2.** A comparison of the mean temperatures from this work and those of Ikebe et al. (2002), showing the line of equality.

expression for  $r_{500}$ , we have not allowed for the effects of evolution in the overdensity factor (i.e. the ‘500’) with redshift. However, for such a low-redshift sample, the impact of this evolution is negligible.

The mean cluster temperature,  $\bar{T}$ , is measured from the spectrum extracted within  $0.1-0.2r_{500}$ , thus excluding the central region where the effects of strong gas cooling can contaminate the X-ray emission. The combination of  $\bar{T}$  and  $r_{500}$  is determined iteratively, by extracting an initial spectrum, finding the best-fitting temperature, then using this to estimate  $r_{500}$ , and repeating the process until convergence is achieved.

Fig. 2 shows a comparison of the mean temperatures derived with those from the original *ASCA* analysis of Ikebe et al. (2002), who used a two-temperature fit to correct for the effects of any CC. There is good agreement below  $\sim 5$  keV, but above this our temperatures are systematically hotter in almost every case, for both CC and non-CC clusters. However, this behaviour is most likely the result of differences in the regions from which spectra were extracted in the two analyses. The most massive clusters have large angular sizes, which are significantly larger than the *Chandra*, but not *ASCA*, field of view. Since the temperature almost always declines beyond any CC (e.g. Markevitch 1998; Piffaretti et al. 2005; Vikhlinin et al. 2005), this would lead to a higher mean temperature measured with *Chandra*.

#### 4.2 Cool core clusters

Having determined the cluster mean temperature, unbiased by the effects of central gas cooling, the spectrum of the core region ( $<0.1r_{500}$ ) was extracted separately and fitted as before to yield a core temperature (see Table 2). A comparison between this core temperature and the mean (core-excluded) temperature can then be used to quantify the influence of central cooling. By considering the

**Table 2.** Detailed properties of the sample, listed in order of increasing temperature.

Name	Mean $kT$ (keV)	Core $kT^a$ (keV)	$kT$ ratio <sup>b</sup>	$R_{500}$ (kpc)	CC significance <sup>c</sup>	BM type	Notes <sup>d</sup>
NGC 5044	$1.19^{+0.03}_{-0.02}$	$0.88^{+0.00}_{-0.00}$	$1.35^{+0.03}_{-0.03}$	$437^{+6}_{-6}$	11.7*	–	C, F
Abell 262	$2.34^{+0.06}_{-0.06}$	$1.82^{+0.02}_{-0.02}$	$1.28^{+0.04}_{-0.04}$	$667^{+11}_{-11}$	7.9*	III	C
Abell 4038	$3.02^{+0.17}_{-0.17}$	$3.26^{+0.14}_{-0.13}$	$0.93^{+0.07}_{-0.07}$	$785^{+28}_{-28}$	–1.1	III	–
Abell 1060	$3.19^{+0.07}_{-0.07}$	$3.40^{+0.04}_{-0.05}$	$0.94^{+0.02}_{-0.02}$	$811^{+12}_{-12}$	–2.6	III	–
Abell 1367	$3.28^{+0.11}_{-0.10}$	$3.32^{+0.10}_{-0.09}$	$0.99^{+0.04}_{-0.04}$	$826^{+17}_{-16}$	–0.3	II–III	M, R
2A0335+096	$3.47^{+0.14}_{-0.12}$	$2.34^{+0.03}_{-0.03}$	$1.48^{+0.06}_{-0.06}$	$857^{+22}_{-18}$	8.2*	–	C, F, M
Abell 2147	$4.17^{+0.14}_{-0.14}$	$4.82^{+0.37}_{-0.19}$	$0.87^{+0.06}_{-0.06}$	$961^{+20}_{-20}$	–2.3	III	M
Abell 2199	$4.36^{+0.13}_{-0.11}$	$3.93^{+0.04}_{-0.04}$	$1.11^{+0.03}_{-0.03}$	$989^{+18}_{-15}$	3.4*	I	C
Abell 496	$5.91^{+0.58}_{-0.56}$	$3.58^{+0.11}_{-0.11}$	$1.65^{+0.17}_{-0.17}$	$1197^{+75}_{-70}$	3.9*	I	F
Abell 2256	$6.08^{+0.30}_{-0.31}$	$5.64^{+0.45}_{-0.50}$	$1.08^{+0.11}_{-0.11}$	$1220^{+38}_{-38}$	0.7	II–III	F, M, R
Abell 1795	$6.30^{+0.17}_{-0.17}$	$4.88^{+0.06}_{-0.06}$	$1.29^{+0.04}_{-0.04}$	$1246^{+21}_{-21}$	7.5*	I	C, F
Abell 3558	$6.64^{+0.34}_{-0.51}$	$6.04^{+0.32}_{-0.31}$	$1.10^{+0.09}_{-0.09}$	$1288^{+42}_{-62}$	1.1	I	–
Abell 85	$6.65^{+0.14}_{-0.14}$	$4.80^{+0.06}_{-0.06}$	$1.38^{+0.03}_{-0.03}$	$1290^{+17}_{-17}$	11.4*	I	F, M, R
Abell 3571	$6.71^{+0.15}_{-0.42}$	$7.85^{+0.17}_{-0.17}$	$0.85^{+0.04}_{-0.04}$	$1297^{+19}_{-51}$	–3.6	I	M
Abell 3667	$7.39^{+0.27}_{-0.27}$	$6.76^{+0.18}_{-0.42}$	$1.09^{+0.06}_{-0.06}$	$1378^{+32}_{-32}$	1.5	I–II	F, M, R
Abell 478	$7.97^{+0.18}_{-0.18}$	$6.00^{+0.07}_{-0.07}$	$1.33^{+0.03}_{-0.03}$	$1446^{+21}_{-21}$	9.6*	–	C, F
Abell 401	$8.35^{+0.43}_{-0.61}$	$8.21^{+0.50}_{-0.63}$	$1.02^{+0.09}_{-0.09}$	$1488^{+48}_{-68}$	0.2	I	M
Abell 2029	$9.11^{+0.20}_{-0.20}$	$7.18^{+0.07}_{-0.07}$	$1.27^{+0.03}_{-0.03}$	$1572^{+21}_{-21}$	8.9*	I	F
Abell 2142	$9.45^{+0.65}_{-0.65}$	$7.81^{+0.33}_{-0.33}$	$1.21^{+0.10}_{-0.10}$	$1610^{+71}_{-69}$	2.1	II	F, M
Abell 3266	$9.86^{+0.53}_{-0.54}$	$9.48^{+0.37}_{-0.37}$	$1.04^{+0.07}_{-0.07}$	$1653^{+57}_{-57}$	0.6	I–II	M

<sup>a</sup>The core temperature measured within  $0.1r_{500}$ . <sup>b</sup>Ratio of mean to core temperature. <sup>c</sup>Number of sigma difference from unity (CC clusters are marked with ‘\*’). <sup>d</sup>Clusters with detectable cavities in the ICM are marked with ‘C’, cold front clusters are marked with ‘F’, probable merger clusters are marked with ‘M’, and clusters with radio relics are marked with ‘R’. All errors are 68 per cent confidence.

ratio of the mean to the core temperature as a discriminator, we define CC clusters as those systems for which this ratio exceeds unity at greater than  $3\sigma$  significance. This provides a clean separation of the sample into nine CC and 11 non-CC clusters, with a mean ratio and standard deviation of 1.35/0.15 and 1.0/0.11, respectively.

For comparison, in a recent *Chandra* study Bauer et al. (2005) found that at least 55 per cent of their sample of 38 X-ray luminous clusters show signs of mild cooling, with 34 per cent displaying evidence of strong cooling. According to the definition used by Bauer et al., all the clusters in our sample could be classified as having a CC (cooling time,  $t_{\text{cool}} < 10$  Gyr). However, their sample is more distant ( $z \sim 0.15\text{--}0.4$ ), and they are correspondingly less able to resolve the inner parts of the ICM where the gas cooling time is lowest and possibly falls below 10 Gyr in many cases. The older study of Peres et al. (1998) reported a CC fraction of 70 per cent, based on lower-resolution *ROSAT* observations of a complete sample of the 55 brightest clusters in the sky in the 2–10 keV band. However, their definition of a CC is different again, requiring that the upper limit to the central  $t_{\text{cool}}$  be less than the assumed age for the cluster.

In any case, both Bauer et al. (2005) and Peres et al. (1998) based their definition of a CC on the gas cooling time which, as they demonstrated, is clearly capable of reaching low values ( $\sim$ few Gyr) in most – perhaps all – clusters (see also Section 6.2). By casting our definition in terms of a significant temperature decrease in the inner  $0.1r_{500}$ , we are able to identify clusters where radiative cooling has demonstrably impacted the gas properties in a substantial way, beyond merely forming at least some gas with a low cooling time.

### 4.3 Spectral profiles and deprojection analysis

In order to study the spatial variation of gas temperature, a projected temperature profile was obtained for each cluster. Spectra were extracted in a series of concentric annuli, centred on the peak of the X-ray emission. The radial bins were chosen to enclose a fixed number of net cluster counts between 1000 and 3000, depending on the quality of the observation. Each spectrum was fitted with an absorbed APEC model, as above, to yield the best-fitting temperature. A characteristic radius was assigned to each annulus using the emission-weighted approximation of McLaughlin (1999),

$$r = \left[ 0.5 \left( r_{\text{out}}^{3/2} + r_{\text{in}}^{3/2} \right) \right]^{2/3}. \quad (3)$$

To derive estimates of the three-dimensional gas temperature, we used the XSPEC PROJECT model to deproject the spectral profiles under the assumption of spherical geometry. The deprojection is quite slow and susceptible to strong noise fluctuations, so we used a smaller number of coarser annular bins – between 10 and 20, according to data quality. To stabilize the fitting, the absorbing column and gas metallicity we fixed at values obtained by fitting each annulus separately prior to the deprojection. For some clusters, it was necessary to freeze the absorbing column at the Galactic H I value (as detailed in Table 1), since unfeasibly low values were otherwise obtained in many of the annular bins. However, we verified that in those bins where the absorbing column was able to be fitted, the optimum values were fully consistent with the H I-inferred measurement. Moreover, we found no indication of any radial trend in absorbing column in these cases, which might point to problems with the calibration. Similarly, in a number of cases the deprojected temperature had to be fixed at its projected value, to produce a stable fit (denoted by a ‘T’ in the rightmost column of Table 1). However, these are all non-CC clusters, with approximately isothermal temperature pro-

files, where the smoothing effects of projection are minimal, thus any bias introduced by this approximation is likely to be small.

## 5 NOTES ON INDIVIDUAL CLUSTERS

In this section, we provide further information about each of the clusters in the sample, highlighting key aspects of the analysis specific to different data sets.

### 5.1 NGC 5044

This is the only galaxy group in the sample, since a selection based on flux biases towards more massive clusters. It is a well-studied object, which hosts a cold front and cavities seen in X-ray emission (Buote et al. 2003).

### 5.2 Abell 262

A known cavity cluster (Blanton et al. 2004). The optical properties of this cluster are unusual, and its luminosity function and colour–magnitude relation show signs of contamination from a large number of lower-mass galaxies, possibly associated with a nearby supercluster (W. Barkhouse, private communication).

### 5.3 Abell 4038

It was necessary to use the projected temperature profile in place of the deprojected one for this cluster, in order to stabilize the fitting and thereby avoid strong fluctuation between adjacent bins.

### 5.4 Abell 1060

Optical observations indicate that A1060 has a dynamically perturbed condensed core (Girardi et al. 1997). However, no obvious merger activity is evident from the X-ray emission, so this cluster has not been classified as a merger candidate in Table 1. The projected  $T(r)$  data were used for the deprojection, to avoid strong fluctuations in the recovered profile.

### 5.5 Abell 1367

This is a complex structured cluster, which is clearly undergoing multiple merging, as seen in both optical (e.g. Cortese et al. 2004) and X-rays (Sun & Murray 2002). The projected  $T(r)$  data were used for the deprojection, to avoid strong fluctuations in the recovered profile.

### 5.6 2A0335+096

This is known to be a cold front cluster (Mazzotta, Edge & Markevitch 2003), which also possesses a radio-lobe cavity (Birzan et al. 2004). A recent deep *XMM-Newton* analysis of this system indicates that it is also likely to be undergoing a merger with a subcluster (Werner et al. 2006).

### 5.7 Abell 2147

This cluster is composed of several clumps, with evidence of luminosity segregation in the galaxies (Lugger 1989); it has thus been labelled as a merger candidate in Table 1. It is interesting to note that the brightest cluster galaxy for A2147 is not located at the centre of the cluster potential (and X-ray peak) (Lugger 1989).

It was necessary to fix the absorbing column at the Galactic H I value, since unfeasibly low values were obtained when it was left free to vary. The projected  $T(r)$  data were used for the deprojection, to avoid strong fluctuations in the recovered profile.

### 5.8 Abell 2199

This is a known cavity cluster (Johnstone et al. 2002).

### 5.9 Abell 496

This cluster hosts a prominent cold front (Dupke & White 2003).

### 5.10 Abell 2256

This is a probable cold front cluster in the early stages of merging (Sun et al. 2002). Our annular spectral bins were centred on the main (East) cluster peak, referred to as ‘P1’ in the analysis of Sun et al. (2002).

It was necessary to use the projected  $T(r)$  for the deprojected  $T(r)$ , to avoid strong fluctuations in the deprojected profile, arising from a complicated ‘S’ shaped profile. The absorbing column was also fixed at the Galactic H I value for all bins, to stabilize the fitting; there is no evidence from the global spectrum of any significant difference between the fitted column and the H I value. It was necessary to use the older CIAO task ‘MKRMF’ to generate spectral responses for this data set.

### 5.11 Abell 1795

This is a cold front cluster (Markevitch, Vikhlinin & Mazzotta 2001).

### 5.12 Abell 3558

It was necessary to use the projected  $T(r)$  for the deprojected  $T(r)$  for this cluster.

### 5.13 Abell 85

A well-known subclump cluster, which also has a cold front and is a probable merger candidate (Kempner, Sarazin & Ricker 2002). The prominent Southern subclump and the Western subclump both were excluded from the analysis.

### 5.14 Abell 3571

This cluster is probably in the late stages of merging (Venturi et al. 2002) and is located in the Shapley supercluster. It was necessary to use the projected  $T(r)$  for the deprojected  $T(r)$ .

### 5.15 Abell 3667

This is both a cold front and a merging cluster (Vikhlinin, Markevitch & Murray 2001). It was necessary to use the projected  $T(r)$  for the deprojected  $T(r)$ .

### 5.16 Abell 478

This well-known CC cluster hosts a cold front (Markevitch, Vikhlinin & Forman 2003) and possesses prominent X-ray cavities with coincident radio lobes (Sun et al. 2003).

### 5.17 Abell 401

This is a probable merger remnant (Sakelliou & Ponman 2004). The older CIAO task ‘MKRMF’ was used to create a spectral response matrix, owing to lack of calibration data for the newer task ‘MKACIS-RMF’. It was necessary to use the projected  $T(r)$  for the deprojected  $T(r)$ .

### 5.18 Abell 2029

Another well-studied CC cluster which possesses a cold front (Markevitch et al. 2003).

### 5.19 Abell 2142

This is the archetypal ‘cold-front’ cluster, which likely consists of the largely intact core of a poor cluster enclosed within a halo of much hotter gas associated with a larger cluster (Markevitch et al. 2000). This fact accounts for its unusual temperature profile, which is atypical of non-CC clusters (see Section 6.1).

The two observations of Abell 2142 (ObsIDs 1196 and 1296) were amongst the very first made by *Chandra*, and were taken when the CCD temperature was only  $-100^{\circ}\text{C}$ . Since the standard CIAO calibration does not cover this CCD temperature, these data sets were analysed according to the calibration for a CCD temperature of  $-110^{\circ}\text{C}$ . In addition, the corresponding Markevitch period A blank-sky background data sets are truncated at 10 keV, so the background renormalization was performed in the range 8–10 keV. The analysis presented here is based on the 1196 data set, but to verify our results we also analysed the 1296 observation, and found very good agreement between the density and temperature profiles. As for A401, it was necessary to use the older CIAO task ‘MKRMF’ to generate spectral responses for this data set.

### 5.20 Abell 3266

This is a well-known merging cluster (Henriksen & Tittley 2002). It was necessary to use the projected  $T(r)$  for the deprojected  $T(r)$ .

## 6 RESULTS

### 6.1 Temperature profiles

The temperature profiles from the projected annular analysis are plotted separately for each cluster in Fig. 3, with the vertical dotted lines indicating the region  $0.1-0.2r_{500}$  used to calculate the mean temperature. To clarify the underlying trend in each profile, the raw data points have been fitted with a locally weighted regression in the log–log space, using a method similar to that outlined in Sanderson et al. (2005). This technique effectively smoothes the data using a quadratic function which is moved along the set of points to build up a curve, in an analogous fashion to the way a moving average is computed for a time-series. The algorithm used is implemented in the ‘LOESS’ function in version 2.3 of the R PROJECT statistical environment package<sup>4</sup> (R Development Core Team 2006), which also provides an estimate of the  $1\sigma$  error on the regression, based on the scatter about the curve. To compare profiles across the sample, the projected temperatures are plotted as a function of physical radius (in kpc) for CC and non-CC clusters in separate panels in Fig. 4. Once again the curves represent a locally weighted regression, this time using the R PROJECT ‘LOWESS’ function (as used in Sanderson et al. 2005), which provides a larger degree of smoothing. The curves have been assigned an arbitrary line style to uniquely identify each system.

The difference between CC and non-CC clusters is very clear from Fig. 4. Within the CC, there is a remarkable consistency in shape of the temperature profile, which follows a power law with

<sup>4</sup> <http://www.r-project.org>.

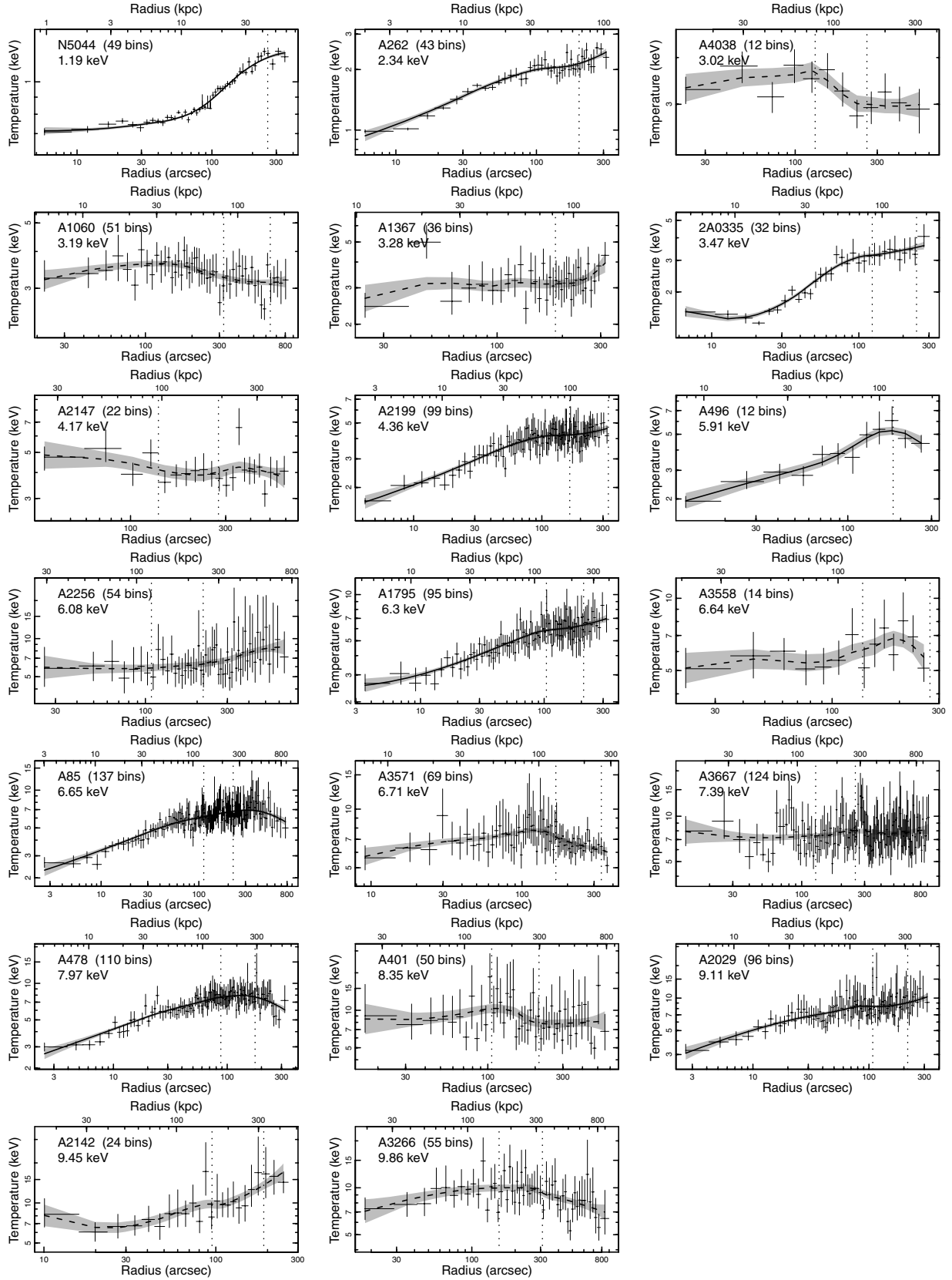


**Figure 3.** Projected temperature profiles and  $1\sigma$  error envelopes for each system, ordered by increasing mean temperature from the top left-hand panel to bottom right-hand panel. The curves represent a locally weighted fit to the data points (in the log–log space). CC clusters are denoted by the solid lines and non-CC clusters are plotted with the dashed lines. The vertical dotted lines bracket the region  $0.1\text{--}0.2r_{500}$ , within which the mean temperature is measured. The mean temperature for each cluster is indicated, as is the number of annular bins used to construct the curves.

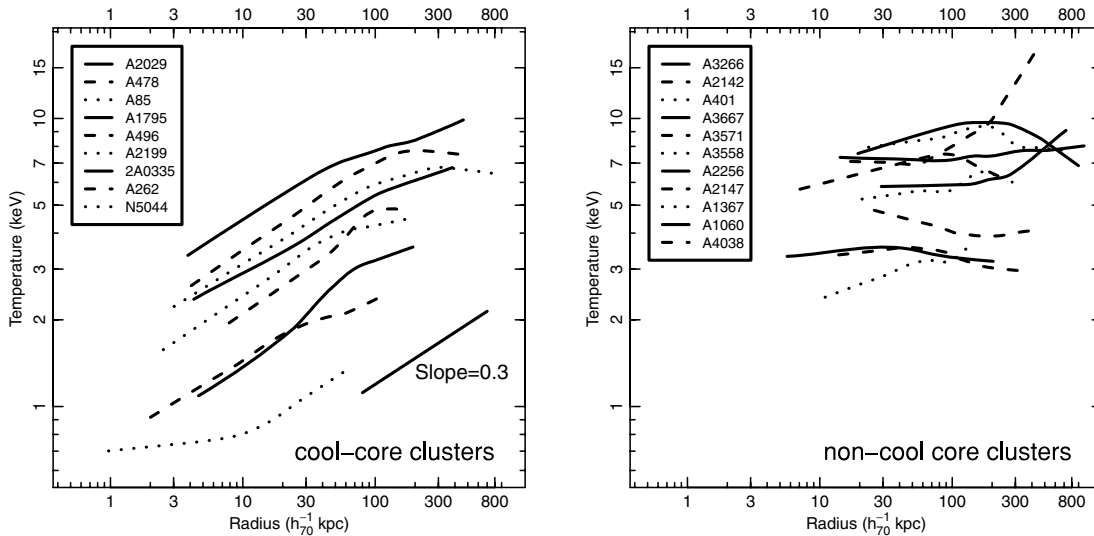


**Figure 4.** Projected, finely binned temperature profiles for the sample, split by CC type and using an arbitrary line style to uniquely identify each system: the cluster name entries in the legends are ordered by temperature. Both plots are scaled identically in temperature and radius. Each curve represents a locally weighted fit to the data points (in the log–log space), to suppress scatter (see the text for details).

a logarithmic slope of roughly 0.3. In most clusters, this behaviour appears to extend down to a few kiloparsecs – well within the central galaxy. The obvious exception to this is the coolest system, the NGC 5044 group, which exhibits a sharp break at  $\sim 10$  kpc, as the logarithmic slope flattens within the central galaxy. As this is the only galaxy group in the sample, this result may point to a different scaling of hot gas at small mass scales. However, this system does display evidence of multiphase gas and morphological disturbances, in the form of X-ray cavities from AGN activity as well as a cold front (Buote et al. 2003). It is therefore possible that this flattening in  $T(r)$  is an atypical feature. However, we emphasize that the possibility of a flattening of  $T(r)$  in the innermost core of clusters (as recently claimed by Donahue et al. 2006, for example) is not ruled out by our data, since the ‘LOWESS’ regression tends to mask such behaviour, by downweighting any deviations of the innermost few points from the general trend. This disadvantage is compensated for by the clarity with which the local regression captures the underlying trend in  $T(r)$ , to highlight the scaling between different clusters.

Fig. 5 shows the variation in projected temperature with scaled radius. The size of the CC region appears to be reasonably well approximated by  $0.1r_{500}$  – the radius of the core exclusion region used in calculating the mean cluster temperature (Section 4.1). However, any turnover in the temperature profile at larger radius is difficult to detect, given the limited field of view of the main *Chandra* detectors. This is compounded by the fact that all but one of the CC cluster observations analysed here used the ACIS-S detector, which covers one-fourth of the area of ACIS-I. A further systematic difference is evident at smaller radii, where the profiles in Fig. 4 extend further in for CC clusters, as a consequence of the bright CC enabling finer annular binning.

The individual deprojected *scaled* temperature profiles are plotted in Fig. 6, as a function of scaled radius. Here, each profile has been normalized by the mean temperature of the cluster, to provide a direct comparison between systems of different masses. It is clear that there is a tight spread between the CC clusters, which hold to an approximately power-law form, with a logarithmic slope of  $\sim 0.4$  (plotted as a solid line with arbitrary normalization). Conversely, the

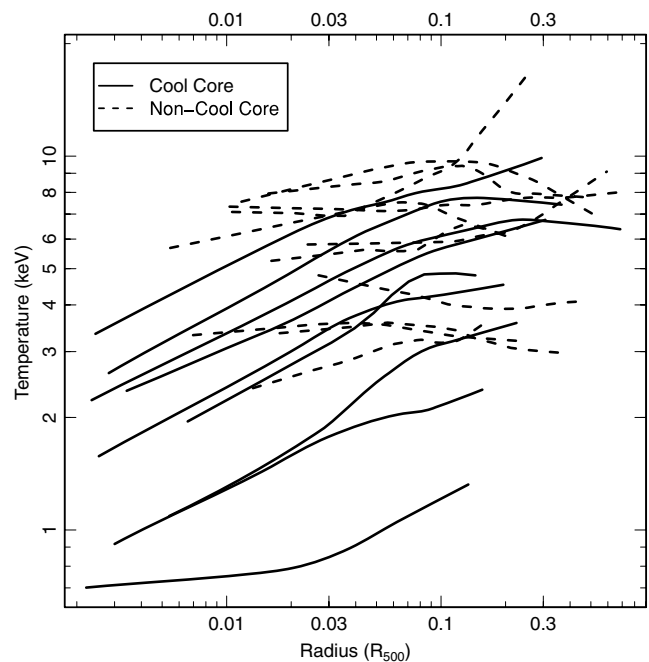


**Figure 5.** Projected, finely binned temperature profiles for each of the clusters, scaled to  $r_{500}$  and labelled according to the presence of a CC. Each curve represents a locally weighted fit to the data points, to suppress scatter (see the text for details).

non-CC clusters scatter around the locus of isothermality (dotted line), showing no obvious systematic variation with radius.

Motivated by the uniformity in temperature profiles displayed by the CC clusters, we have combined all the scaled data points for these systems and subjected them to a locally weighted regression, to determine a characteristic average temperature profile. Each cluster’s deprojected temperature profile was scaled by the mean cluster temperature ( $\bar{T}$ ) and corresponding  $r_{500}$ . The regression was performed in the log–log space, using the R PROJECT task ‘LOESS’, in

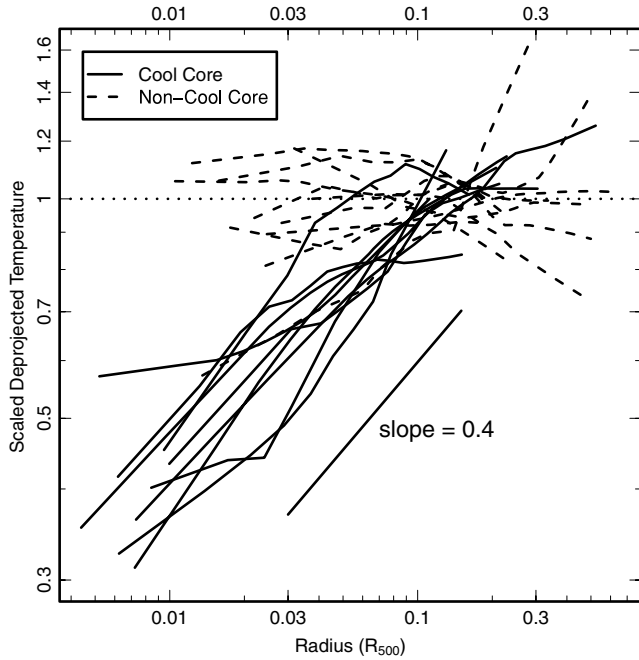


**Figure 6.** Deprojected temperature profiles for CC and non-CC clusters, scaled by  $\bar{T}$  and plotted as a function of scaled radius. Each curve represents a locally weighted fit to the data points, to suppress scatter (see the text for details).

order to provide an estimate of the error on the regression, from the scatter about the line. Each point was weighted by its inverse variance (computed using the mean asymmetric error), to improve the rejection of outliers. The same procedure was applied to the non-CC clusters, to provide a comparison. The corresponding profiles and  $1\sigma$  error envelopes for the CC and non-CC clusters are plotted in Fig. 7. The outermost point has been excluded from the mean CC and non-CC profiles plotted, in order to minimize any bias that this single point can cause at such large radius.

The behaviour of the profiles at large radii is less certain, as indicated by the widening of the regression confidence region, resulting from the diminishing number of points. However, there is clearly a preference for a peak at  $\sim 0.15r_{500}$ , followed by a decline, which is broadly consistent with previous analyses (e.g. Piffaretti et al. 2005; Vikhlinin et al. 2005; Zhang et al. 2006).

## 6.2 Cooling time

A simple estimate of the susceptibility of gas to radiative cooling can be obtained by considering the time-scale over which the gas can continue to lose energy at its current rate. Thus defined, the cooling time (in seconds) of a parcel of gas with volume,  $V$  (in  $\text{cm}^3$ ), and luminosity,  $L_X$  (in  $\text{erg s}^{-1}$ ), is given by

$$t_{\text{cool}} = 1.602 \times 10^{-9} \times \frac{3kT\rho V\mu_e}{2\mu L_X}, \quad (4)$$

where  $kT$  is the *deprojected* gas temperature (in keV),  $\rho$  is the electron number density (in  $\text{cm}^{-3}$ ), and the constants  $\mu_e$  and  $\mu$  are, respectively, the mean mass per electron (1.167) and the mean molecular weight (0.593) of the gas. Profiles of cooling time as a function of scaled radius are plotted in Fig. 8, colour coded by the mean cluster temperature. As before, the curves represent a locally weighted regression to the data points. Note that the cooling time in the outermost annular bin is unknown (unlike the temperature),

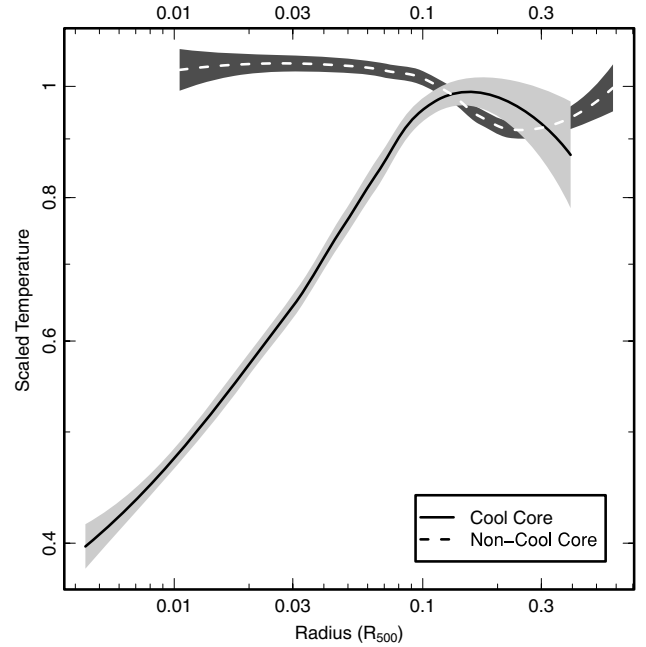


**Figure 7.** Mean deprojected temperature profiles for CC and non-CC clusters, scaled by  $\bar{T}$  and plotted as a function of scaled radius. Each curve represents a locally weighted fit to the data points, to suppress scatter (see the text for details). The shaded regions represent the  $1\sigma$  confidence region of the fit.

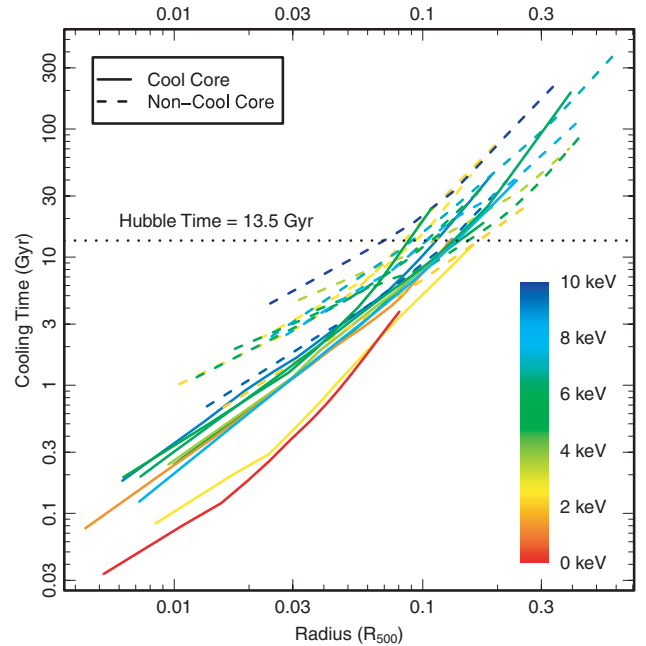


**Figure 8.** Gas cooling time profiles for each of the clusters, scaled to  $r_{500}$ , labelled according to the presence of a CC, and coloured according to the cluster mean temperature. Each curve represents a locally weighted fit to the data points, to suppress scatter (see the text for details).

since the assumed volume is not well defined, which means that the gas density cannot be determined.

For purely bremsstrahlung X-ray emission,  $t_{\text{cool}} \propto \sqrt{kT}$ . However, the contribution of line emission becomes significant at lower temperatures, which weakens this trend. Therefore, this simple scaling has not been applied to Fig. 8, and the profiles are thus largely

ordered by mean cluster temperature. None the less, despite this spread in temperature, there is a clear consistency between all the profiles, with much greater similarity between CC and non-CC clusters than that which is seen at the gas temperature. Not surprisingly, the CC systems have consistently lower cooling times at all radii, but they also exhibit a slightly steeper logarithmic slope than those of the non-CC clusters. While it is clear that CC clusters reach much lower values in the core, it can be seen that within  $\sim 0.1r_{500}$ , most non-CC clusters have rather low cooling times, falling below a Hubble time in all cases.

It can be seen in Fig. 8 that the locus corresponding to the Hubble time intersects the profiles around  $0.1r_{500}$ . This is the same radius as used to excise any cooling-dominated flux from the mean cluster temperature estimates (Section 4.1), and also approximately corresponds to the point where the CC cluster temperature profiles reach a maximum (Fig. 7). It is apparent that even in non-CC clusters, the cooling time of gas within this radius can fall well below a Hubble time. However, the non-CC gas cooling time seems to reach a minimum level of around 1 Gyr, whereas all the CC profiles fall well below this value. To some extent, this behaviour can be explained by the fact that CC clusters permit a much finer scale spectral binning, and so their gas properties can be measured to smaller radii, where  $t_{\text{cool}}$  is naturally lower. Nevertheless, non-CC clusters have notably shallower cooling time profiles at all radii.

An alternative perspective is obtained by studying cooling time as a function of physical rather than scaled radius, as plotted in Fig. 9. Here, the scatter between the profiles is actually reduced, particularly beyond  $\sim 100$  kpc. Moreover, the two largest outliers in Fig. 8 (the coolest two systems) lie well within the main trend, albeit with NGC 5044 showing a significantly steeper outer slope. The implication of this is that the cooling time of gas in virialized systems (either with or without a CC) obeys a universal form across more than two orders of magnitude in radius, with relatively small scatter (a factor of  $\sim 3$ ), as found previously by Voigt & Fabian (2004) and Bauer et al. (2005). This suggests a prominent role for radiative cooling in governing cluster properties. It is not clear exactly why this should

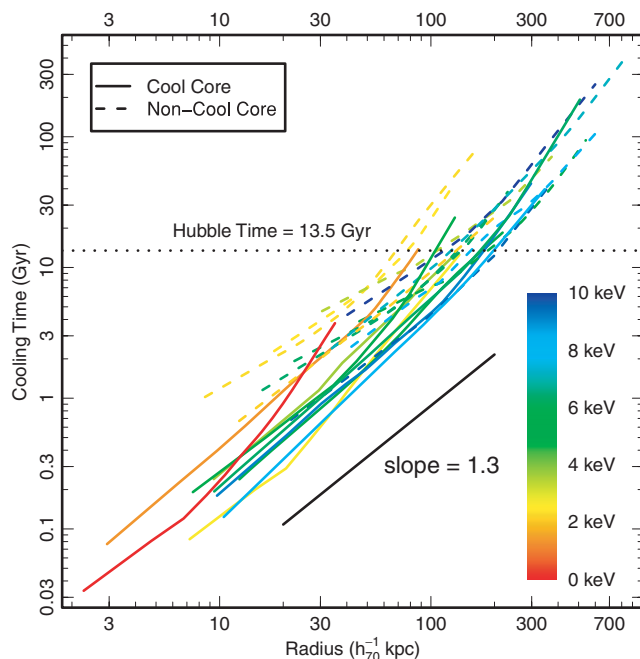


Figure 9. Same as Fig. 8, but plotted as a function of radius in kpc.

be so, but it represents an interesting challenge to theoretical models of cluster properties to account for this behaviour.

Within  $\sim 100$  kpc,  $t_{\text{cool}}$  scales roughly as  $r^{1.3}$ , as indicated by the solid black line, which agrees with the findings of Voigt & Fabian (2004), based on a sample of 16 clusters with strong CCs. A similar result was obtained by Bauer et al. (2005), from a sample of 38 X-ray luminous clusters at moderate redshift. Furthermore, the apparent steepening of the profiles at larger radius is also consistent with both these previous studies.

## 7 DISCUSSION

It is clear that clusters can be subdivided into two distinct categories according to the presence or absence of a CC (e.g. Peres et al. 1998; Bauer et al. 2005). How then can we explain the mixture of these types in the cluster population? Judging from our cooling time results, gas in the cores of all clusters falls well below a Hubble time (down to a least  $\sim 1$  Gyr). This demonstrates that the ICM is certainly capable of developing a CC in the inner regions; that it does not always do so implies the influence of some counteracting process(es).

Given the predominantly isothermal temperature profiles seen amongst the non-CC clusters, it is natural to examine the role of cluster merging in erasing CCs, which would tend to mix gas and smooth out thermal gradients (e.g. Fabian, Nulsen & Canizares 1984; Edge, Stewart & Fabian 1992; Buote & Tsai 1996). The rightmost column of Table 2 indicates which clusters show signs of merging activity, and a clear trend is apparent: eight out of 10 ‘merger’ clusters are non-CC, leaving only three out of 11 non-CC clusters showing no obvious signs of merging, namely Abell 1060, Abell 4048 and Abell 3558. Of these, A1060 has a dynamically perturbed condensed core (Girardi et al. 1997) and may be a relatively recent merger cluster in which a CC has not yet been re-established (Yamasaki, Ohashi & Furusho 2002). The CC clusters with indications of merging activity are Abell 85 and 2A0335+096. Of these, A85 clearly contains two subclusters and it appears that the CC has survived a merger with at least one of these objects (Kempner et al. 2002). A similar event may well be occurring in 2A0335+096 (Werner et al. 2006), thus demonstrating that not all mergers are capable of destroying an existing CC.

If merging is primarily responsible for erasing CCs, then its impact outside this region must be relatively minor. We note that there is no evidence that the non-CC clusters are significantly hotter on average than the CC ones, (e.g. Fig. 1), based on the temperature measured within  $0.1-0.2r_{500}$  (Section 4.1); a comparison of the temperatures of the CC and non-CC clusters, using the Kolmogorov–Smirnov test (implemented in the R PROJECT function ‘KS.TEST’), results in a  $p$ -value of 0.9195 in favour of the null hypothesis that the two sets of data are drawn from the same continuous distribution. It can be seen that the cooling time profiles of both types of cluster roughly converge beyond  $\sim 0.1r_{500}$  (Fig. 8). The head-on merger simulations of Gómez et al. (2002) indicate that the residual signature of a CC may remain for up to 1–2 Gyr after a disruptive merger, before the onset of turbulence heats the gas significantly. Thus, it is possible for a CC cluster to have recently experienced a significant disruption, which could account for the presence of CCs and merger signatures in both A85 and 2A0335+096.

Within the core, the apparent ‘floor’ value of  $\sim 1$  Gyr seen in the cooling time of non-CC clusters could represent the time taken to re-form a CC. If mergers are primarily responsible for erasing CCs, then this time-scale can be linked to the characteristic time-scale between such events. Specifically, the fraction of non-CC

clusters would correspond to the fraction of the time between mergers that is required to re-establish a CC. Therefore, if the  $\sim 1$  Gyr ‘floor’ value represents the time taken to re-form a CC and roughly 50 per cent of the sample possess a CC, this implies a characteristic time of  $\sim 2$  Gyr between mergers. By comparison, the simulations of Cohn & White (2005) indicate that, on average, clusters in their sample of 574 have experienced at least four large mergers since  $z \sim 2$ , corresponding to a lookback time of  $\sim 10$  Gyr. This implies a mean time-scale of roughly 2.5 Gyr between mergers, which is consistent with the above figure.

Alternatively, CCs could be disrupted by AGN-driven outflows originating in the central galaxy, which is a plausible mechanism for explaining their absence (e.g. McNamara et al. 2005; O’Sullivan et al. 2005b) and is capable of mixing up gas (e.g. O’Sullivan, Vrtilik & Kempner 2005a). However, all the six clusters in our sample with obvious evidence of AGN-associated cavities in the ICM (marked with a ‘C’ in the rightmost column of Table 2) possess CCs, reflecting the well-established trend for CC clusters to host central radio sources (Burns 1990). On the other hand, AGN may well play an important role in regulating unchecked cooling in cluster cores, which is well established to be significantly suppressed (Peterson & Fabian 2006, and references therein). If AGN activity contributes towards offsetting cooling in addition to merging, then this would impact the merger rate inferred above. Specifically, any contribution from AGN heating would require correspondingly fewer mergers, thereby increasing the time-scale between such events. In that case, the value of  $\sim 2$  Gyr deduced above would represent a lower limit to the time between major mergers.

For purely bremsstrahlung X-ray emission, the emissivity scales as  $\sqrt{kT}\rho_{\text{gas}}^2$ , which in turn implies  $t_{\text{cool}} \propto \sqrt{kT}$ . Therefore, the apparent universality of the cooling time as a function of physical radius (Fig. 9) indicates that hotter clusters must have a higher gas density (approaching  $\rho_{\text{gas}} \propto \sqrt{kT}$ ). However, a given physical radius corresponds to a smaller fraction of  $r_{500}$  in hotter clusters, which therefore samples gas of higher density, since  $\rho_{\text{gas}}$  generally increases towards the centre. Thus, even if gas at a given fraction of  $r_{500}$  had the same density in clusters of all masses, there would be some reduction in the scatter in  $t_{\text{cool}}$  plotted against physical radius compared to  $r_{500}$ . Nevertheless, a trend for a lower gas density in groups compared to clusters has previously been reported (e.g. Sanderson et al. 2003). Furthermore, the generally good agreement found between the baryon fraction in massive clusters and the ratio of  $\Omega_{\text{b}}/\Omega_{\text{m}}$  (e.g. Allen, Schmidt & Fabian 2002; Sanderson & Ponman 2003), demonstrates that it is the reduced  $\rho_{\text{gas}}$  in less-massive systems that is anomalous.

If clusters and groups form self-similarly at any given epoch from material of constant density, then radiative cooling, or indeed non-gravitational heating – operating more effectively in groups – could have acted to deplete the gas in the centres of groups, thereby lowering the density of the remaining material. However, such a process must have occurred subsequent to collapse and virialization, and so we would expect to observe evidence of systems in an intermediate state, which would register as outliers in Fig. 9. The lack of significant outliers suggests that the implied variation in gas density may already have substantially been in place *prior* to virialization, which implies *non*-self-similar accretion.

Such a scenario is consistent with models in which preheating takes places predominantly in filaments, whose linear geometry causes the energy injected to impact the density in preference to the temperature (as suggested by Ponman, Sanderson & Finoguenov 2003; Voit et al. 2003). Thus, the gas in the smaller filaments feeding small haloes could be ‘puffed up’ more than that in larger cluster

filaments, lowering the density of material accreted on to groups. However, if this picture is correct, it points to an uncomfortable coincidence, namely that preheating of gas prior to accretion and shock heating produces virialized material of roughly constant cooling time at any given physical radius. Such an apparent conspiracy might only be resolved if some fundamental connection between preheating and cooling in haloes could be established.

### 7.1 Mergers, radio relics and cold fronts

Many clusters are known to possess large-scale, diffuse radio sources which are related to the ICM rather than AGN (Giovannini & Feretti 2004). Such sources emit synchrotron radiation, and are referred to as radio relics. Of the clusters in this sample, four are classified as radio relics, namely Abell 85 (Giovannini & Feretti 2000), Abell 1367 (Gavazzi 1978), Abell 2256 (Rottgering et al. 1994; Clarke & Ensslin 2006) and Abell 3667 (Rottgering et al. 1997). The non-CC cluster Abell 4038 also has a radio halo similar to a relic, but this is most likely the remnant of a radio galaxy now located  $\sim 18$  kpc to the east of the relic (Slee et al. 2001). Similarly, Abell 2142 has a small radio halo which may originate from a single galaxy which was active in the past (Giovannini & Feretti 2000). The generally accepted view is that genuine radio relics (i.e. much larger scale than emission from a single radio galaxy) are the product of shock waves arising from merging activity (Ensslin et al. 1998), and this picture is borne out by the fact that all four of these clusters are merger candidates. However, A85 also possesses a CC, demonstrating that it is possible for a CC to survive a merger energetic enough to produce a radio relic.

A related aspect is the prevalence of cold fronts in the sample, which are found in seven of the CC clusters and three of the non-CC clusters. Out of these 10 cold front clusters, five show signs of merging. Clearly, cold fronts are much more common in CC clusters (7/9) than in non-CC clusters (3/11), which is consistent with the findings of Markevitch et al. (2003), who reported that roughly 70 per cent of the nearby CC clusters in their *Chandra* sample of 37 contained cold fronts. A similar fraction has been found more recently from an *XMM-Newton* analysis of 62 clusters (Ghizzardi et al. 2005). In any case, the presence of cold fronts is certainly not incompatible with the existence of a CC. For very relaxed clusters, like Abell 2029 and Abell 1795, cold fronts may result from the infall of small subhaloes (Ascasibar & Markevitch 2006), rather than being caused by more substantial merging.

### 7.2 Properties of the central galaxy

Most of the clusters in this sample possess a large central galaxy which is coincident with the X-ray peak. The presence of this additional potential well is likely to impact the cluster properties in the core, so here we briefly explore the characteristics of the central galaxy. The Bautz–Morgan (BM) classification scheme (Bautz & Morgan 1970) was devised to catalogue clusters of galaxies according to the contrast between the central galaxy and the other galaxies in the cluster (see Bahcall 1977, for a review). There are three main categories, which are defined as follows.

- (i) Type I are clusters containing a centrally located cD galaxy.
- (ii) Type II are clusters where the brightest members are intermediate in appearance between cD galaxies and Virgo- or Coma-type normal giant ellipticals.
- (iii) Type III are clusters containing no dominant galaxies.

Although the BM type is a subjective quantity, which is susceptible to bias (Leir & van den Bergh 1977), it none the less provides a reasonable measure of the evolutionary state of the cluster. BM classifications are available for 17 of the 20 clusters in the sample (the three unclassified systems are Abell 478, NGC 5044 and 2A0335+096) and are listed in Table 2. A total of five out of the six CC clusters with a BM classification contain Type I central galaxies, compared to only three out of 11 non-CC clusters. Moreover, the only CC cluster with a non-Type I classification is an anomalous system: Abell 262 (Type III) exhibits a very unusual colour–magnitude relation and luminosity function, with an apparent large excess of fainter galaxies, consistent with significant contamination from a background supercluster (W. Barkhouse, private communication).

It is clear that BM Type I clusters are more evolved than Types II and III, in the sense that they are unlikely to have experienced significant recent disruption. The tendency for CC clusters to be BM Type I, and non-CC clusters to be Types II and III is therefore consistent with the hypothesis that merger activity removes or otherwise prevents the formation of a CC. This behaviour is consistent with the findings of Buote & Tsai (1996), who discovered a tendency for larger BM types to show evidence of global morphological disturbance in the form of a larger power ratio. Similarly, Ledlow et al. (2003) found that earlier BM types tend to have higher X-ray luminosities, consistent with their hosting CCs, confirming the trend for CC clusters to have an early BM type discovered by Edge & Stewart (1991a).

While the merger hypothesis has received support from observational studies (e.g. Allen et al. 2001) as well as earlier simulations (e.g. Ricker & Sarazin 2001; Ritchie & Thomas 2002), the viability of cluster merging destroying CCs has recently been called into question (Gómez et al. 2002; Motl et al. 2004; Poole et al. 2006). The detailed investigation of Poole et al. (2006) indicates that simulations of even head-on, equal-mass mergers are incapable of disrupting an existing compact CC, either by heating or by mixing of gas. Poole et al. attributed this new development in part to a better treatment of gas cooling in their simulations, which had initially been neglected (Roettiger, Loken & Burns 1997; Ricker & Sarazin 2001). Furthermore, they incorporated empirically motivated initial conditions for their merging clusters (outlined in McCarthy et al. 2004), which result in more realistic and compact progenitor CCs than those in the study of Ritchie & Thomas (2002), for example, who nevertheless modelled the effects of radiative cooling.

On the face of it, these new results of Poole et al. appear to rule out the possibility of CCs ever being disrupted. However, this raises the question of why CCs are not ubiquitous, given that the gas in all the non-CC clusters in this sample reaches cooling times as low as a few Gyr, although here are a number of possible explanations for this (see e.g. the recent review of Peterson & Fabian 2006, and references therein). Moreover, the tendency for non-CC clusters to show signs of recent disruption in the form of radio relics and a Type II/III BM classification is not otherwise easily understood. Finally, it must be remembered that radiative cooling and feedback are notoriously difficult processes to model in numerical simulations, and that even the most sophisticated schemes may fail to adequately capture subtle, small-scale physics of the sort that could significantly affect gas dynamics in cluster merging.

Irrespective of any causal relationship between merging activity and the presence of a CC, the distinctive properties of the latter reinforce the notion of an intrinsic bimodality within the cluster population. Such a conclusion has important implications for the use of scaling relations as a tool for estimating cluster properties, such as mass, since any bimodality would likely dominate the scatter

in these relations (see e.g. O’Hara et al. 2006). The extent to which this bimodality extends to the fundamental property of mass will be addressed in a follow-up paper.

## 8 CONCLUSIONS

We have studied a statistically selected sample of 20 clusters and groups of galaxies, drawn from the flux-limited catalogue of Ikebe et al. (2002), using data from the *Chandra* X-ray satellite. The data have been analysed using a non-parametric deprojection technique, to estimate the three-dimensional temperature and density structure of the ICM. We define a quantitative method to determine the extent to which cooling influences cluster properties: a CC cluster is defined as one where the ratio of the mean temperature within  $0.1-0.2r_{500}$  to that within  $0.1r_{500}$  exceeds unity at  $>3\sigma$  significance. Accordingly, we find that the sample contains nine CC and 11 non-CC clusters.

We find that there is a clear difference between CC and non-CC clusters, with the latter exhibiting somewhat heterogeneous properties, although tending to be roughly isothermal within their inner regions. CC clusters, in contrast, display a remarkable uniformity in the shape of their inner temperature profiles. The cooling time profiles display greater uniformity across the sample, with non-CC clusters tending to possess longer cooling times at all radii, with a slightly flatter logarithmic slope. Nevertheless, even non-CC clusters have cooling times much lower than a Hubble time in all cases. This fact, together with the high incidence of merger activity found amongst the non-CC clusters, indicates that the gas mixing and shock heating that this entails may be responsible for erasing CCs or inhibiting their formation. When the gas cooling time is plotted as a function of radius in physical units, there is a surprising decrease in the scatter between different clusters, indicative of a universal cooling time profile for gas in collapsed haloes. This result suggests that radiative cooling plays a significant role in establishing cluster properties.

## ACKNOWLEDGMENTS

AJRS thanks Joe Mohr, Wayne Barkhouse and Alessandro Gardini for useful discussions and suggestions. We are grateful to the referee for suggestions which have improved this paper. AJRS acknowledges partial support from NASA awards NNG05GI62G and GO5-6129X and from PPARC, and EO acknowledges support from NASA award AR4-5012X. This work made use of the NASA/IPAC Extragalactic Database (NED).

## REFERENCES

- Allen S. W., Fabian A. C., Johnstone R. M., Arnaud K. A., Nulsen P. E. J., 2001, *MNRAS*, 322, 589
- Allen S. W., Schmidt R. W., Fabian A. C., 2002, *MNRAS*, 334, L11
- Ascasibar Y., Markevitch M., 2006, *ApJ*, in press (astro-ph/0603246)
- Bîrzan L., Rafferty D. A., McNamara B. R., Wise M. W., Nulsen P. E. J., 2004, *ApJ*, 607, 800
- Bahcall N. A., 1977, *ARA&A*, 15, 505
- Bauer F. E., Fabian A. C., Sanders J. S., Allen S. W., Johnstone R. M., 2005, *MNRAS*, 359, 1481
- Bautz L. P., Morgan W. W., 1970, *ApJ*, 162, L149
- Blanton E. L., Sarazin C. L., McNamara B. R., Clarke T. E., 2004, *ApJ*, 612, 817
- Buote D. A., Tsai J. C., 1996, *ApJ*, 458, 27
- Buote D. A., Lewis A. D., Brighenti F., Mathews W. G., 2003, *ApJ*, 594, 741

- Burns J. O., 1990, *AJ*, 99, 14
- Clarke T. E., Ensslin T. A., 2006, *AJ*, 131, 2900
- Cohn J. D., White M., 2005, *Astropart. Phys.*, 24, 316
- Cortese L., Gavazzi G., Boselli A., Iglesias-Paramo J., Carrasco L., 2004, *A&A*, 425, 429
- Dickey J. M., Lockman F. J., 1990, *ARA&A*, 28, 215
- Donahue M., Horner D. J., Cavagnolo K. W., Voit G. M., 2006, *ApJ*, 643, 730
- Dupke R., White R. E., 2003, *ApJ*, 583, L13
- Edge A. C., Stewart G. C., 1991a, *MNRAS*, 252, 428
- Edge A. C., Stewart G. C., 1991b, *MNRAS*, 252, 414
- Edge A. C., Stewart G. C., Fabian A. C., 1992, *MNRAS*, 258, 1772
- Ensslin T. A., Biermann P. L., Klein U., Kohle S., 1998, *A&A*, 332, 395
- Fabian A. C., Nulsen P. E. J., Canizares C. R., 1984, *Nat*, 310, 733
- Finoguenov A., Reiprich T. H., Böhringer H., 2001, *A&A*, 368, 749
- Fukazawa Y., Makishima K., Ohashi T., 2004, *PASJ*, 56, 965
- Gavazzi G., 1978, *A&A*, 69, 355
- Ghizzardi S., Molendi S., Leccardi A., Rossetti M., 2006, in Wilson A., ed., *ESA SP-604, The X-ray Universe 2005*. ESA Publications Division, Noordwijk
- Giovannini G., Feretti L., 2000, *New Astron.*, 5, 335
- Giovannini G., Feretti L., 2004, *J. Korean Astron. Soc.*, 37, 323
- Girardi M., Escalera E., Fadda D., Giuricin G., Mardirossian F., Mezzetti M., 1997, *ApJ*, 482, 41
- Gómez P. L., Loken C., Roettiger K., Burns J. O., 2002, *ApJ*, 569, 122
- Grevesse N., Sauval A. J., 1998, *Space Sci. Rev.*, 85, 161
- Helsdon S. F., Ponman T. J., 2000, *MNRAS*, 315, 356
- Henriksen M. J., Tittley E. R., 2002, *ApJ*, 577, 701
- Ikebe Y., Reiprich T. H., Böhringer H., Tanaka Y., Kitayama T., 2002, *A&A*, 383, 773
- Johnstone R. M., Allen S. W., Fabian A. C., Sanders J. S., 2002, *MNRAS*, 336, 299
- Kempner J. C., Sarazin C. L., Ricker P. M., 2002, *ApJ*, 579, 236
- Ledlow M. J., Voges W., Owen F. N., Burns J. O., 2003, *AJ*, 126, 2740
- Leir A. A., van den Bergh S., 1977, *ApJS*, 34, 381
- Lugger P. M., 1989, *ApJ*, 343, 572
- Markevitch M., 1998, *ApJ*, 504, 27
- Markevitch M., Forman W. R., Sarazin C. L., Vikhlinin A., 1998, *ApJ*, 503, 77
- Markevitch M. et al., 2000, *ApJ*, 541, 542
- Markevitch M., Vikhlinin A., Forman W. R., 2003, in Bowyer S., Hwang C.-Y., eds, *ASP Conf. Ser. Vol. 301, A High Resolution Picture of the Intracluster Gas*. Astron. Soc. Pac., San Francisco, p. 37
- Markevitch M., Vikhlinin A., Mazzotta P., 2001, *ApJ*, 562, L153
- Mazzotta P., Edge A. C., Markevitch M., 2003, *ApJ*, 596, 190
- McCarthy I. G., Balogh M. L., Babul A., Poole G. B., Horner D. J., 2004, *ApJ*, 613, 811
- McLaughlin D. E., 1999, *AJ*, 117, 2398
- McNamara B. R., Nulsen P. E. J., Wise M. W., Rafferty D. A., Carilli C., Sarazin C. L., Blanton E. L., 2005, *Nat*, 433, 45
- Motl P. M., Burns J. O., Loken C., Norman M. L., Bryan G., 2004, *ApJ*, 606, 635
- O'Hara T. B., Mohr J. J., Bialek J. J., Evrard A. E., 2006, *ApJ*, 639, 64
- O'Sullivan E., Vrtilik J. M., Kempner J. C., 2005a, *ApJ*, 624, L77
- O'Sullivan E., Vrtilik J. M., Kempner J. C., David L. P., Houck J. C., 2005b, *MNRAS*, 357, 1134
- Peres C. B., Fabian A. C., Edge A. C., Allen S. W., Johnstone R. M., White D. A., 1998, *MNRAS*, 298, 416
- Peterson J. R., Fabian A. C., 2006, *Phys. Rep.*, 427, 1
- Piffaretti R., Jetzer P., Kaastra J. S., Tamura T., 2005, *A&A*, 433, 101
- Ponman T. J., Sanderson A. J. R., Finoguenov A., 2003, *MNRAS*, 343, 331
- Poole G. B., Fardal M. A., Babul A., McCarthy I. G., Quinn T., Wadsley J., 2006, *MNRAS*, in press (doi: 10.1111/j.1365-2966.2006.10916.x) (astro-ph/0608560)
- R Development Core Team 2006, *R: A Language and Environment for Statistical Computing*. R Foundation for Statistical Computing, Vienna, Austria
- Reiprich T. H., Böhringer H., 2002, *ApJ*, 567, 716
- Ricker P. M., Sarazin C. L., 2001, *ApJ*, 561, 621
- Ritchie B. W., Thomas P. A., 2002, *MNRAS*, 329, 675
- Roettiger K., Loken C., Burns J. O., 1997, *ApJS*, 109, 307
- Rottgering H., Snellen I., Miley G., de Jong J. P., Hanisch R. J., Perley R., 1994, *ApJ*, 436, 654
- Rottgering H. J. A., Wieringa M. H., Hunstead R. W., Ekers R. D., 1997, *MNRAS*, 290, 577
- Sakelliou I., Ponman T. J., 2004, *MNRAS*, 351, 1439
- Sanderson A. J. R., Ponman T. J., 2003, *MNRAS*, 345, 1241
- Sanderson A. J. R., Ponman T. J., Finoguenov A., Lloyd-Davies E. J., Markevitch M., 2003, *MNRAS*, 340, 989
- Sanderson A. J. R., Finoguenov A., Mohr J. J., 2005, *ApJ*, 630, 191
- Slee O. B., Roy A. L., Murgia M., Andernach H., Ehle M., 2001, *AJ*, 122, 1172
- Sun M., Murray S. S., 2002, *ApJ*, 576, 708
- Sun M., Murray S. S., Markevitch M., Vikhlinin A., 2002, *ApJ*, 565, 867
- Sun M., Jones C., Murray S. S., Allen S. W., Fabian A. C., Edge A. C., 2003, *ApJ*, 587, 619
- Venturi T., Bardelli S., Zagaria M., Prandoni I., Morganti R., 2002, *A&A*, 385, 39
- Vikhlinin A., Markevitch M., Murray S. S., 2001, *ApJ*, 551, 160
- Vikhlinin A., Markevitch M., Murray S. S., Jones C., Forman W., Van Speybroeck L., 2005, *ApJ*, 628, 655
- Voigt L. M., Fabian A. C., 2004, *MNRAS*, 347, 1130
- Voit G. M., Balogh M. L., Bower R. G., Lacey C. G., Bryan G. L., 2003, *ApJ*, 593, 272
- Werner N., de Plaa J., Kaastra J. S., Vink J., Bleeker J. A. M., Tamura T., Peterson J. R., Verbunt F., 2006, *A&A*, 449, 475
- Willis J. P. et al., 2005, *MNRAS*, 363, 675
- Yamasaki N. Y., Ohashi T., Furusho T., 2002, *ApJ*, 578, 833
- Zhang Y., Böhringer H., Finoguenov A., Ikebe Y., Matsushita K., Schuecker P., Guzzo L., Collins C. A., 2006, *A&A*, in press (astro-ph/0603275)

This paper has been typeset from a  $\text{\TeX}/\text{\LaTeX}$  file prepared by the author.